TENTH AUSTRALASIAN FLUID MECHANICS
CONFERENCE - UNIVERSITY OF MELBOURNE
11-15 DECEMBER 1989

NUMERICAL INVESTIGATION OF HYPERSONIC EXHAUST PLUME/AFTERBODY FLOW FIELDS

T.A. EDWARDS

NASA Ames Research Center
Moffett Field, California 94035
USA

ABSTRACT

An upwind, implicit Navier-Stokes computer program has been applied to hypersonic exhaust plume/afterbody flow fields. The sensitivity of gross thrust to operating conditions has been assessed through parametric variations. Comparison of the numerical results with available experimental data shows good agreement in all cases investigated. Results show that for moderately underexpanded jets, the afterbody force varies linearly with the nozzle exit pressure. Exhaust gases with low isentropic exponents (γ) were found to contribute up to 25% more afterbody force than high-γ exhaust gases. Modifying the nozzle geometry influenced the exhaust plume development, which had a significant effect on the afterbody force. Grid density, while important to resolving the initial plume/afterbody interaction, had only a minor impact on the resultant afterbody force.

INTRODUCTION

Hypersonic flight is a vital link in the advancement of transportation within and beyond the earth's atmosphere. Efficient flight at hypersonic speeds requires a new approach to airbreathing propulsion: the supersonic combustion ramjet (scramjet) engine. The aerodynamics of scramjet propulsion can be described in three components: 1) forebody compression, 2) internal fuel injection and ignition, and 3) afterbody expansion. Compressing the flow on the forebody is accomplished when the oncoming air traverses the bow shock of the vehicle. This creates a dense, high pressure flow at the engine inlet. The internal segment of the scramjet propulsion cycle consists of further flow compression, followed by fuel injection and ignition. The final stage of the scramjet cycle, which is crucial to its performance, is the flow of underexpanded exhaust gases leaving the nozzle.

This paper studies the details of an important determinant of scramjet performance: impingement of the engine exhaust plume on the underbody. Since the exhaust flow is, in general, highly underexpanded, it exerts high pressure on the lower surface of the afterbody, which yields additional thrust. However, small deviations from design conditions could easily lead to inadequate engine performance. Predicting performance at and away from the design point requires new computational analysis tools.

The goal of the present work is to demonstrate a CFD capability to solve complex nozzle/afterbody problems in hypersonics, and to investigate the fluid dynamics of underexpanded exhaust plumes as they impinge on vehicle afterbodies. First, the governing equations and numerical solution methods are described. Flow solutions for a nozzle/afterbody model are presented and compared to experimental data. Next, the sensitivity of nozzle performance to several parameters is assessed. Finally, the effect of grid density on the numerical results is investigated.

GOVERNING EQUATIONS AND NUMERICAL METHOD

The thin-layer, Reynolds averaged Navier-Stokes equations provide a good model for the flow conditions considered here. These equations are solved in generalized curvilinear coordinates, as presented in Pulliam et al. (1978), for example. Gas leaving scramjet nozzles possesses markedly different thermodynamic properties than the external flow, and these differences must be accounted for in the governing equations. As a first approximation, this is accomplished by solving a species continuity equation in conjunction with the Navier-Stokes equations. The diffusion terms are neglected because their effect on the afterbody force is negligible compared to the convective terms for the present analysis. Thus, the species continuity equation is written as

$$\frac{\partial c}{\partial t} + u\frac{\partial c}{\partial x} + v\frac{\partial c}{\partial y} + w\frac{\partial c}{\partial z} = 0 \qquad (1)$$

The velocity components u, v, and w correspond to the Cartesian coordinate directions x, y, and z, respectively; t designates time, and c is the mass fraction of the exhaust gas. For binary mixtures, only one species equation needs to be solved. That information, in connection with the global continuity equation, provides closure.

The species continuity equation is coupled to the Navier-Stokes equations through γ, the ratio of specific heats. After determining the exhaust gas mass fraction by solving the species continuity equation, the equivalent γ, designated $\tilde{\gamma}$, is found from

$$\tilde{\gamma} = \frac{cc_{p_1} + (1-c)c_{p_2}}{cc_{v_1} + (1-c)c_{v_2}} \qquad (2)$$

where c_v, c_p are the specific heats. The subscript 1 refers to the exhaust gas properties, and 2 to the external flow properties. The ideal gas equation of state remains unchanged except that γ is replaced by $\tilde{\gamma}$. Thus, the pressure p is determined from

$$p = (\tilde{\gamma} - 1)\left[e - \frac{1}{2}\rho(u^2 + v^2 + w^2)\right] \qquad (3)$$

where e is the total energy and ρ is the density.

The Navier-Stokes equations are solved with an algorithm developed by Rai (1986), which employs a flux splitting scheme due to Steger et al. (1981) for the implicit flux terms, and an upwind TVD scheme due to Roe (1983) for the explicit flux terms. The species continuity equation cast in the form of Eq. (1) results in a scalar partial differential equation. To solve this numerically, one-sided spatial

differencing is applied according to the local flow velocity. The equation is approximately factored so that it may be solved with scalar tridiagonal inversions in each of the three coordinate directions. For a more complete description of the computational approach, see Edwards (1988).

SIMULATION OF EXHAUST PLUME FLOW FIELDS

To study the effects of exhaust plume/afterbody interactions and calibrate the numerical method, the surface geometry and flow conditions were chosen to correspond to a wind tunnel experiment of a simple nozzle/afterbody model. This experiment provided data on the sensitivity of the afterbody force to some governing parameters, such as nozzle exit pressure ratio and exhaust gas properties. The results of the numerical solutions are presented and discussed below.

Nozzle/Afterbody Model

model description. The experimental model under consideration was analyzed by Cubbage et al. (1971), and had as its goal measurement of the lift, drag, and pitching-moment increments resulting from the impingement of an underexpanded exhaust plume on a flat plate. The model, shown in figure 1, consists of an inlet/nozzle assembly attached to a flat plate that represents a hypersonic vehicle underbody. The plate is hinged at the nozzle exit plane to simulate varying afterbody upsweep angles. Boundary layer trips were placed downstream of the leading edge to insure turbulent flow over the rest of the body. The tests were conducted in the Langley 20-inch Mach 6 tunnel at a stagnation pressure of 25 atm and a stagnation temperature of 480 K. The Reynolds number was 20.9×10^6 per meter. Instrumentation consisted of pressure taps placed in a grid pattern downstream of the nozzle assembly in the jet expansion region.

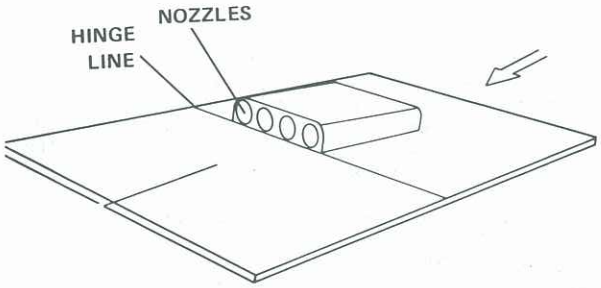

Figure 1. Nozzle/afterbody model schematic.

Two axisymmetric nozzle geometries were tested with the flat plate model, one of which was designed for air ($\gamma = 1.4$), and the other for a gas mixture of 75% sulfur hexaflouride (SF_6) and 25% nitrogen (N_2) by weight, so chosen to yield an isentropic exponent, γ, of 1.26 at the nozzle exit plane. This mixture was chosen because it is relatively inert and stable, producing a dense, energetic gas akin to frozen flow in an actual flight condition. The nozzles were designed to produce nearly the same momentum flux and Mach number at the nozzle exit plane for both gases. A "two-dimensional", or slot nozzle was also tested with air as the exhaust gas. Air flowing into the inlet of the nozzle assembly was exhausted outside the test section, while the nozzle flow was supplied by a high pressure reservoir. Pressure data were reported along the model centerline (between the two inner nozzles) and on the centerline of an outboard nozzle.

grid generation. The computational domain for the nozzle/afterbody model was discretized with a Cartesian grid topology. Grid dimensions were 60 in the stream direction, 33 in the span direction, and 62 normal to the afterbody, for a total of 122,760 points. The solution domain includes only the part of the model downstream of the exhaust nozzles, and bilateral symmetry was assumed across the model centerline. The nozzle geometry was not modeled explicitly in the grid; rather, the effect of the nozzle flow (and surrounding solid surfaces) was accounted for through the inflow boundary conditions.

flow field description. Underexpanded jets in a supersonic freestream exhibit readily identifiable flow structures. Upon leaving the nozzle, the flow "expands" by turning toward the region of lower pressure. The adjacent supersonic external flow is forced to turn also, and an oblique shock wave (the plume shock) emanates from the nozzle lip. Meanwhile, an expansion fan propagates into the plume flow, eventually contacting and reflecting off of the afterbody surface. This flow pattern is evident in the numerical solutions. For example, figure 2 shows the calculated pressure contours on the plate, at the symmetry plane of the model, and at the inflow plane. Flow conditions for this solution were $M_\infty = 6$, $\alpha = 0°$, $Re = 209{,}000\ \text{cm}^{-1}$, and $\epsilon = 0°$, where ϵ designates the afterbody upsweep angle. The nozzle exit pressure ratio (p_e/p_∞) is 6.23, and the exit Mach number is 3.5. At the inflow plane, pressure contours outline the nozzle circumferences. The plume shock is also readily evident in this view at the symmetry plane. Pressure peaks on the plate are apparent near the nozzle lip (where the exhaust flow first impinges on the plate), and further downstream where adjacent plumes interact.

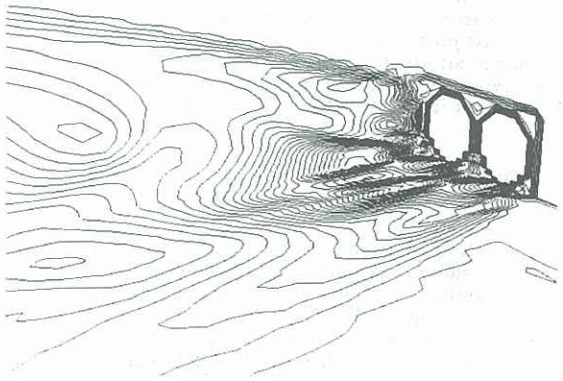

Figure 2. Pressure contours on afterbody and symmetry plane of nozzle/afterbody model at $M_\infty = 6$, $\alpha = 5°$, $p_e/p_\infty = 6.23$.

Surface pressure coefficients are compared with the experimental data at two pressure ratios in figure 3. In figure 3(a), the pressure along the model centerline is seen first to rise due to shock impingement at $x/d \approx 1.5$; it then falls to near ambient pressure at $x/d \approx 5$. The shock is the result of adjacent plumes interfering with one another as they expand to ambient pressure. Further downstream, the flow overexpands, and at $x/d \approx 6$, a recompression is apparent. The comparison in this figure is generally good, though the strength of the first shock is underpredicted somewhat. This is due in part to the discrete modeling of the round nozzles, and improved results using a finer grid are described below. Figure 3(b) shows the surface pressure coefficients on the centerline of the outboard nozzle. The pressure falls rapidly from its value at the exit plane, then reaches a plateau which occurs at $x/d \approx 1$ in the experimental data, and at $x/d \approx 2$ in the calculated result. The pressure plateau occurs where the expansion of the exhaust plume is restricted by interference with the adjacent plume. Downstream of this point, the flow becomes slightly overexpanded, then recovers to ambient pressure.

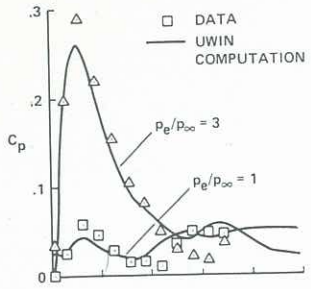

(a) between nozzles

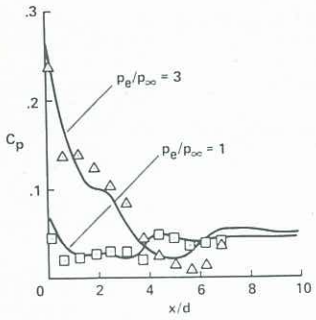

(b) nozzle centerline

Figure 3. Comparison of calculated and experimental surface pressure coefficients for nozzle/afterbody model. $M_\infty = 6$, $\alpha = 5°$.

Parametric Effects on Afterbody Forces

Numerous parameters affect the magnitude and direction of force arising from the impingement of the exhaust plume on the afterbody. The nozzle/afterbody model permitted analysis of some of the dominant variables. In this section, an investigation of parametric sensitivities is opened. Parameters studied include the nozzle exit pressure ratio, exhaust gas properties, and nozzle geometry.

pressure ratio. To assess the sensitivity of the afterbody normal force to the exit pressure ratio, flow solutions for the nozzle/afterbody model were obtained at otherwise fixed operating conditions with variations in exit pressure ratio from 1 to 4. The incidence of the model to the free stream, α, was 0°, and the afterbody upsweep, ϵ, was also 0° for these solutions. Figure 4 presents the normal force coefficient as a function of the nozzle exit pressure ratio. The comparison of the numerical results with the data is very good, and the model exhibits a linear relationship between exit pressure and normal force, as expected: other things equal, an increase in the nozzle exit pressure gives rise to a corresponding increase in pressure on the region of the plate downstream of the nozzles. Hence, the force on the plate rises in direct proportion to the nozzle exit pressure.

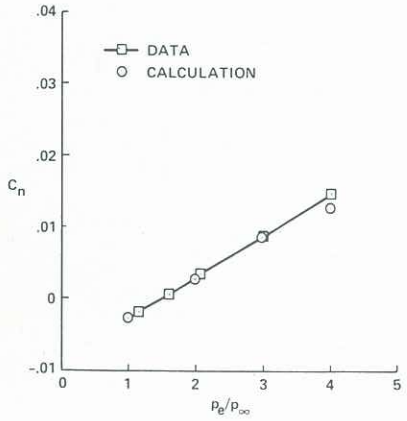

Figure 4. Variation of normal force coefficient with exit pressure ratio. $M_\infty = 6$, $\alpha = 0°$.

exhaust gas properties. Coupling a species continuity equation to the Navier-Stokes equations made it possible to model the effect that different (ideal) exhaust gases have on the afterbody force. The isentropic exponent, γ, was initialized to 1.4 everywhere except the nozzle exit, where it was given a value of 1.26, corresponding to the exhaust gas tested in the experiment. A lower value of γ indicates more internal energy modes; hence, the gas requires a greater volumetric expansion to achieve a given reduction in pressure.

Figure 5 shows the effect this has on the afterbody flow field. At $\alpha = 0°$, $\epsilon = 0°$, $p_e/p_\infty = 4$, the footprint for the SF_6 exhaust gas is notably larger than for air: it persists an additional nozzle diameter downstream, and it spreads laterally by about another one-half nozzle diameter. The pressure within the SF_6 footprint is higher as well; for this case, the normal force for $\gamma_e = 1.26$ was about 25% higher than for $\gamma_e = 1.4$. Results showed that the variation of normal force coefficient with exit pressure ratio is still linear, but the slope is about 30% greater for $\gamma_e = 1.26$ than for $\gamma_e = 1.4$. Therefore, at the same exit conditions, a gas with a low value of γ will produce a greater afterbody force than one with a high value of γ.

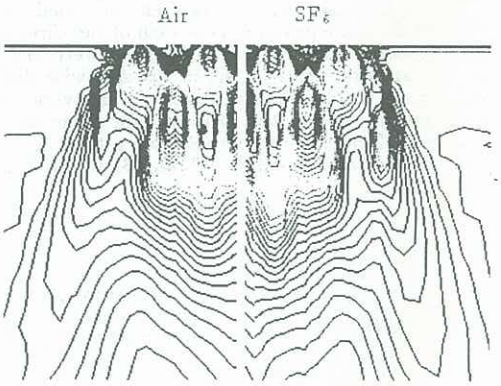

Figure 5. Comparison of pressure contours on afterbody for SF_6 exhaust gas and air. $M_\infty = 6$, $\alpha = 0°$.

nozzle geometry. To investigate the effect of nozzle geometry on the afterbody flow field, a slot nozzle was tested for comparison with the axisymmetric nozzle geometry. The slot nozzle was designed to produce the same momentum flux as the axisymmetric nozzles. The test conditions were $\alpha = 5°$, $\epsilon = 0°$, and $p_e/p_\infty = 6.23$.

Comparisons of the calculated surface pressure coefficients with experimental data for the slot nozzle are shown in figure 6. The plume expansion is more uniform and persists two nozzle diameters further downstream than the axisymmetric nozzle flow. The centerline pressure for the slot nozzle is seen to be consistently underpredicted from $x/d = 0$ to $x/d \approx 5$. This is thought to be a result of two discrepancies between the experiment and the numerical model: 1) nonuniform experimental exit flow conditions, causing a pressure peak near the exit face, and 2) geometrical disparity, causing the predicted onset of expansion to

occur about one nozzle diameter upstream of the experimentally determined location.

In contrast to the recirculating flow near the exit plane of the axisymmetric nozzles, the slot nozzle was found to produce an unseparated, nearly two-dimensional flow field in the plume footprint on the afterbody. This had a significant effect on the afterbody normal force: $c_{n_{slot}} = .0778$, while $c_{n_{axi}} = .0409$.

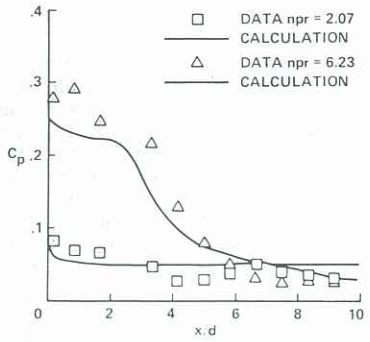

Figure 6. Comparison of calculated and experimental surface pressure coefficients for slot nozzle geometry. $M_\infty = 6$, $\alpha = 5°$.

Grid Resolution Effects

As a necessary final step to the nozzle/afterbody investigation, the convergence of the numerical results is tested on a series of grids. To minimize the effects of unequal grid stretching on the results of this study, results were first obtained on a fine grid, which was then coarsened twice by discarding alternate grid points in each of the three coordinate directions. The fine grid dimensions were 119 points in the streamwise direction, 63 in the spanwise direction, and 123 in the plate-normal direction, for an overall total of 922,131 points. Hence, the medium grid dimensions were 60, 33, and 62 points, respectively, for a total of 122,760 points; the coarse grid had 31, 17, and 31 for 16,337.

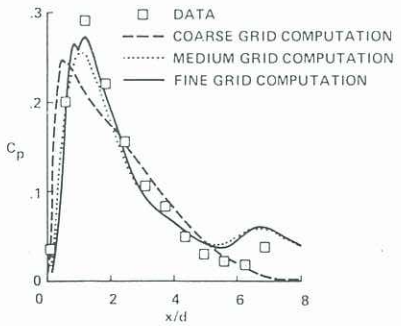

Figure 7. Comparison of calculated surface pressure coefficients on model centerline. $M_\infty = 6$, $\alpha = 5°$, $p_e/p_\infty = 6.23$.

Pressure coefficient comparisons among solutions on the three grids are shown in figure 7. The coarse grid result follows the broad trends in the data, but fails to place the interference peak correctly, and shows no evidence of recompression at $x/d = 6$. The medium and fine grid results are nearly identical to one another, though the fine grid result shows a higher interference peak.

Significant differences in the recirculating flow field near the nozzle exit plane were noted for the refined grid solutions. The solution on the coarse grid indicated no flow separation at all, while the two finer grids showed differing separation patterns where the adjacent exhaust plumes impinged on the plate. On the nozzle centerline, all the results were identical, indicating that even the coarse grid adequately captures regions of attached flow. Resolving the recirculating flow field near the nozzle exit would require a finer grid and enhanced physical models.

However, plate force measurements were not especially sensitive to grid density. Plate normal force coefficients, shown in Table 1, indicate an asymptotic trend toward a value of about 0.138. The medium grid dimensions, which were used for the other nozzle/afterbody grids as well, produced results within about 10% of the asymptotic value.

Table 1. Effect of grid density on plate normal force. $M_\infty = 6$, $\alpha = 5°$, $\epsilon = 0°$, $p_e/p_\infty = 6.23$.

Grid	Dimensions	Total Points	c_n
Coarse	$31 \cdot 17 \cdot 31$	16,337	0.1009
Medium	$60 \cdot 33 \cdot 62$	122,760	0.1256
Fine	$119 \cdot 63 \cdot 123$	922,131	0.1362

CONCLUSION

The capability to solve numerically the interaction of an underexpanded exhaust plume with a vehicle afterbody has been demonstrated. The numerical results compared favorably with experimental data for several operating conditions. The afterbody force, which is an important propulsion performance index, varies linearly with the nozzle exit pressure. The exhaust gas composition has also been shown to influence the afterbody force. The nozzle geometry was found to affect the initial plume development, affecting the resulting afterbody force as well. While the flow characteristics near the nozzle exit show a great deal of sensitivity to the grid resolution, the afterbody force was found to be well predicted with the grids used in this study.

REFERENCES

CUBBAGE, J.M. Jr., and KIRKHAM, F.S. (1971) Investigation of Engine-Exhaust-Airframe Interference on a Cruise Vehicle at Mach 6. NASA TN D-6060.

EDWARDS, T.A. (1988) The Effect of Exhaust Plume/-Afterbody Interaction on Installed Scramjet Performance. NASA TM-101033.

PULLIAM, T.H., and STEGER, J.L.(1978) On Implicit Finite-Difference Simulations of Three Dimensional Flow. AIAA paper no. 78-10.

RAI, M.M., and CHAKRAVARTHY, S. (1986) An Implicit Form for the Osher Upwind Scheme. AIAA Journal Vol. 24, No. 5, pp. 735-743.

ROE, P.L. (1983) Approximate Riemann Solvers, Parameter Vectors, and Difference Schemes. J. Comp. Phys. 43, pp. 357-372.

STEGER, J.L., and WARMING, R.F. (1981) Flux-Vector Splitting of the Inviscid Gas Dynamic Equations with Applications to Finite Difference Methods. J. Comp. Phys. 40, pp. 263-293.